Regular Article - Atomic Physics

Investigation of the atomic structure of curium and determination of its first ionization potential

Nina Kneip[1,2,a], Felix Weber[1], Magdalena A. Kaja[1], Christoph E. Düllmann[2,3,4], Christoph Mokry[2,3], Sebastian Raeder[3,4], Jörg Runke[2,4], Dominik Studer[1], Norbert Trautmann[2], and Klaus Wendt[1]

[1] Institut für Physik, Johannes Gutenberg-Universität Mainz, 55099 Mainz, Germany
[2] Department Chemie - Standort TRIGA, Johannes Gutenberg Universität Mainz, 55099 Mainz, Germany
[3] Helmholtz-Institut Mainz, 55099 Mainz, Germany
[4] GSI Helmholtzzentrum für Schwerionenforschung GmbH, 64291 Darmstadt, Germany

Abstract. We report on the investigation of the atomic structure of curium ($Z = 96$) by resonance ionization spectroscopy. Three different excited energy levels were populated from the $5f^7 6d7s^2 \, ^9D_2^o$ ground state as first excitation steps. Wide-range scans were performed for the search of second excitation steps around the literature value of the ionization potential. These spectra were analyzed to identify Rydberg levels and auto-ionizing resonances. The ionization potential was consistently determined as $48330.68(16)\,\mathrm{cm}^{-1}$ through the evaluation of Rydberg convergences and the complementary approach of DC electric field ionization by evaluating the ionization threshold according to the saddle point model. The new result deviates by $6.7\,\mathrm{cm}^{-1}$ from the literature value of $48324(2)\,\mathrm{cm}^{-1}$ by Köhler et al. [15] and is about one order of magnitude more precise.

1 Introduction

The element curium ($Z = 96$) is exclusively man-made and was discovered in 1946 by the group around Glenn T. Seaborg [1]. At that time, the isotope ^{242}Cm was produced by bombarding ^{239}Pu with α-particles [2]. Curium is present in spent nuclear fuel with about 20 g/ton, produced by successive neutron capture and β^--decays from ^{238}U [3]. To date, curium isotopes from ^{233}Cm to ^{251}Cm are known, of which the isotopes $^{242-248}$Cm and ^{250}Cm exhibit long half-lives in the order of 1 up to 10^7 years [4]. These allow for a variety of spectroscopic studies in this element. Curium isotopes are relevant in the field of radioanalytics and radio protection, e.g., after the Chernobyl reactor accident in 1986. In this context, ^{242}Cm ($T_{1/2} = 162.6$ d) is one of the strongest α-particle emitters and is 14 times more active than, e.g., ^{239,240}Pu [5]. Thus, curium appears as a major component of the radiotoxic nuclear fallout.

The accurate determination of the total curium content and isotope ratios is in addition relevant for nuclear proliferation, but also for other fields, e.g., transmutation attempts as well as for the safe disposal of this particularly long-lived radioactive waste constituent. In this field, Gorietti *et al.* studied metal waste samples with different radiochemical and analytical methods,

e.g., ICP-MS[1] and α-spectrometry to determine the relevant plutonium and americium/curium isotope ratios [6]. Resonant Laser-Secondary Neutral Mass Spectrometry (rL-SNMS) is a new and well-suited method to quantitatively determine curium contents including precise isotope ratios with spatial resolution in small particles and on surfaces. This technique has been successfully applied for ultra-sensitive and highly element-selective analyses of radiotoxic isotopes including the actinide isotopes ^{236,238}U, $^{238-242}$Pu, ^{241,243}Am, and ^{99}Tc [7,8]. Highly efficient and element-selective ionization schemes are crucial for a high sensitivity and to suppress isobaric interferences, e.g., observed in the cases of ^{238}U versus ^{238}Pu, ^{243}Am versus ^{243}Pu, or ^{242}Am versus ^{242}Cm. Such schemes must be identified in all elements of interest by laser spectroscopy [9]. For this, detailed information about the atomic structure of the respective element must be collected.

On the other hand, laser spectroscopy is a highly suitable method for the study of atomic spectra, specifically in combination with a resonant laser ionization step for efficient ion production. The high efficiency and element selectivity of two- or three-step resonance ionization spectroscopy (RIS) makes it particularly suitable for such studies on minuscule sample amounts down to the picogram level [10]. Across the periodic table, the highest spectral line density is found in the lan-

---

[a] e-mail: nina.kneip@uni-mainz.de (corresponding author)

[1] **I**nductively **C**oupled **P**lasma-**M**ass **S**pectrometry.

thanides and actinides, having an open f-shell in the atomic ground state (GS). In particular, actinide spectra are strongly influenced by relativistic effects as well as intense electron correlations and corresponding configuration interactions [11].

In the curium atom (Cm I), Worden *et al.* spectroscopically identified more than 13 000 lines, which they assigned to 335 odd and 348 even parity levels pointing out its enormous atomic level density and the resulting complexity of the curium atomic structure [12,13]. They used 2mg of ^{244}Cm ($T_{1/2} = 18.10$y) and performed the measurement at the large 9.15m Paschen Runge spectrograph of Argonne National Laboratory.

The ionization potential (IP) of curium was first estimated by interpolating the IPs of other actinides to $E_{IP,Interp.} = 49100(200)$cm^{-1} [14]. It was measured in 1996 with the electric field ionization (FI) technique in three-step RIS to $E_{IP,FI} = 48324(2)$cm^{-1} [15]. This method applying the classical saddle point model is ideally suited to extract the IP from the complex atomic spectra of actinides, where convergences of Rydberg series may not be easily identified due to high spectral density and disturbances from configuration interactions.

In this work, ionization schemes were developed performing laser spectroscopy of high lying states and AI resonances around the first IP of curium. The identification of Rydberg states leads to a re-determination of the IP of the curium atom via two-step RIS. The IP value was determined by analyzing the Rydberg series and additionally confirmed by using the electric field ionization method.

2 Experimental setup

The experiment to determine the IP of curium through Rydberg convergences was carried out at the off-line radioactive ion beam facility RISIKO[2] at Mainz University. Experimental details on the RISIKO mass separator can be found in [16]. The development of three RIS schemes as well as the final FI studies was performed at the MABU[3] apparatus, as described in [9], while more details relevant for the individual measurements will be given in the according sections. A simplified sketch of the experimental setup of both devices showing the individual components is given in Fig. 1. The MABU is less sensitive compared to the 30keV RISIKO mass separator due to the low acceleration potential of just ∼ 200V and the limited transmission of the 90° deflector and the quadrupole mass filter.

The Mainz Ti:sapphire laser system was used to excite and ionize the sample atoms. As a pump laser, a commercial Nd:YAG laser at 532nm with a pulse repetition rate of 10kHz and a power of about 14W per Ti:sapphire laser was used. The wavelength was
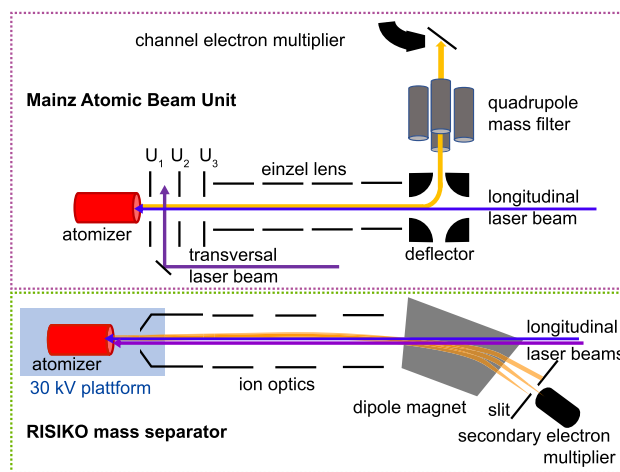
---

[2] **R**esonance **I**onization **S**pectroscopy **I**n **K**ollinear Ge**O**metry.
[3] **M**ainz **A**tomic **B**eam **U**nit.

Fig. 1 Schematic sketch of the experimental setups used for the experiments. **Top:** The Mainz atomic beam unit (MABU), involving 90° ion beam deflection and a quadrupole mass filter. It was used for ionization scheme development as well as for IP determination by field ionization (FI). **Bottom:** The RISIKO mass separator with a 60° sector field magnet used for spectroscopic studies of the Rydberg series

selected by a birefringent filter in combination with a thin etalon in case of the standard Ti:sapphire laser and by a reflective grating on a fully automated rotation stage for the tunable Ti:sapphire laser [18]. The second harmonics was generated in both laser types by an intra-cavity BBO[4] crystal. The scan speed and the power of the tunable Ti:sapphire laser were computer-controlled over the whole scan range. The frequency-doubled laser average output power reaches up to 1.2 W in case of the standard Ti:sapphire laser and up to 400 mW for the tunable Ti:sapphire laser. The tunable laser had a spectral linewidth of 2GHz and the standard laser of typically 7GHz. The fundamental wavelengths of the lasers were measured by using a High Finesse WSU-30 wavemeter, which has an absolute uncertainty of 30MHz. The actual accuracy corresponds to 20% of the laser beam width, i.e., ≈ 0.12cm^{-1}. For the measurements with higher spectral resolution, an additional etalon was inserted into the laser resonator, reducing the linewidth to slightly below 1GHz [19].

At RISIKO, samples with $2 \cdot 10^9$ atoms of ^{248}Cm were used. The material was dissolved in nitric acid and pipetted onto a 5×5 mm^2 zirconium foil of 25μm thickness. After evaporation of the liquid, the sample was folded and placed into the ion source, which is a tantalum tube of 350mm length and 2.5mm inner diameter. It also serves as a confinement of the laser ionization region. The tube was heated stepwise up to 2300K. The first curium signal was detected at a temperature of about 1700K. In addition to resonant laser ionization, atoms were also ionized by contacts with the hot cavity surfaces, producing surface ions. Due to the very efficient and selective resonant laser ionization process,

---

[4] β-bariumborate.

the surface ion contribution to the total signal was only of the order of 1%.

The ionization scheme development was carried out at MABU [9,20], which is equipped with an atomizer geometry similar to the RISIKO mass separator. However, due to the significantly lower transmission of the MABU, larger samples with 2×10^{13} atoms of ^{248}Cm atoms were used. Ions were extracted from the ion source by three extraction electrodes, providing a potential of 200V for acceleration. The electrodes U_1 and U_2 were configured for precise electric field setting for FI. After extraction, the ions were directed towards a 90° electrostatic quadrupole deflector after which they passed a quadrupole mass filter, transmitting ions with a specific mass-over charge ratio. The subsequent detection of single ions was done by a channel electron multiplier. For ionization scheme development, as discussed in the next section, the laser beams were introduced longitudinally into the ion source through the deflector.

3 Excitation schemes

Starting from the odd-parity ground state $5f^7 6d7s^2\,^9D_2^o$, the three even-parity excited states $5f^7 6d7s7p\,^9D_3$ (A), $5f^8 6d7s\,^9D_3$ (B) and $5f^7 6d7s7p\,^7D_2$ (C), located at $23083.19\mathrm{cm}^{-1}$, $24747.71\mathrm{cm}^{-1}$ and $25287.08\mathrm{cm}^{-1}$, were explored. These experimentally determined energies measured in ^{248}Cm are in good agreement with the values from Blaise et al. [22] given for ^{244}Cm, considering IS, which was extrapolated by Worden et al. [21]. Figure 2 shows the investigated ionization schemes at the top and the measured line profiles of the three first excitation steps (FES) at the bottom. FES$_C$ exhibits strong saturation broadening due to high laser power used.

In curium, the odd-parity ground state configuration $5f^7 6d7s^2\,^9D^o$ splits into five low-lying fine-structure components with $J = 2$ to $J = 6$ located at $0\mathrm{cm}^{-1}$, $302.153\mathrm{cm}^{-1}$, $815.655\mathrm{cm}^{-1}$, $1764.268\mathrm{cm}^{-1}$ and $3089.355\mathrm{cm}^{-1}$. In addition, the level scheme exhibits an atomic level with an even-parity configuration $5f^8 7s^2\,^7F_6$ at $1214.203\mathrm{cm}^{-1}$, which also features a significant thermal population in the hot atomizer source. All energy levels are taken from [22]. Across the relevant temperature range of 1700K to 2300K the GS has the highest relative population of 37%, closely followed by the level at $302.153\mathrm{cm}^{-1}$ with populations of 27%. While scanning the laser for the second excitation step (SES), resonant excitations from the other low-lying populated levels could occur and generate additional peaks in the spectra. In such a case, a two-step, one-color non-resonant ionization could occur or the other fixed laser frequency could similarly ionize the atom non-resonantly over the IP, if the total energy is high enough. Both processes occur in the spectrum taken for scheme A as shown in Fig. 3. These artifacts in the ionization spectrum are rather easily distinguished by their narrow and Gaussian line shape compared to the broad
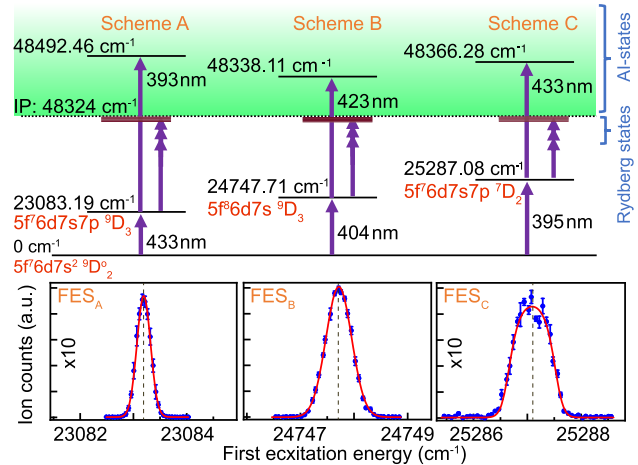

Fig. 2 Two-step RIS scheme in curium. **Top:** The three applied excitation ladders, denoted as schemes A, B and C, are given with their FES and SES. Rydberg and prominent auto-ionizing (AI) state are indicated. **Bottom:** Line profiles of the FES for the three schemes. Intensity in FES$_A$ and FES$_C$ is intensified by a factor of 10

and Fano-shaped profiles of the AIs, and can be specifically selected by scanning the examined range with the SES laser only. This confirmed that the investigated excitation steps indeed start from the GS.

Figure 3 shows the ionization spectrum of scheme A just above the IP using both lasers. Three energy levels were identified as FES, which started from different low-lying levels. Peaks 1 and 2 represent the total excitation energies at $48382.96\mathrm{cm}^{-1}$ and $48414.29\mathrm{cm}^{-1}$. Starting from the low-lying energy level at $302.153\mathrm{cm}^{-1}$ with its electron configuration $5f^7 6d7s^2\,^9D_3^o$, they were identified as FES into energy levels at $24997.81\mathrm{cm}^{-1}$ and $25029.14\mathrm{cm}^{-1}$. Both levels are known and listed with their electron configurations $5f^7 6d7s 7p\,^7D_4$ and $5f^8 6d7s\,^9D_2$ in [22]. Peak 3 was assigned to a FES at $25580.02\mathrm{cm}^{-1}$ with the electron configuration $5f^7 6d7s7p$, $J = 5$, starting from the low-lying level of $5f^7 6d7s^2\,^9D_4^o$ at $815.655\mathrm{cm}^{-1}$ [22]. The few remaining very narrow peaks could be further FES, but were not listed in the tables [13,22] and thus were not investigated further. The AI used for scheme A is highlighted with a yellow box and is the strongest AI level in the entire scan range. It enhances the ion signal by two orders of magnitude compared to non-resonant ionization for this particular ionization scheme.

In direct comparison, scheme B proved to be the most efficient of the three schemes studied for similar laser powers. As determined by non-resonant RIS, the GS transition FES$_B$ to $24747.71\mathrm{cm}^{-1}$ is somewhat stronger than those to FES$_A$ and FES$_C$ to $23083.19\mathrm{cm}^{-1}$ and $25287.08\mathrm{cm}^{-1}$. Scheme A has already been successfully used for RIMS at Mainz University as well as for ultratrace analysis at Hannover University using rL-SNMS [23]. In these studies, scheme A was superior in elemental selectivity, as, e.g., americium was completely suppressed when the lasers were configured for the ioniza-
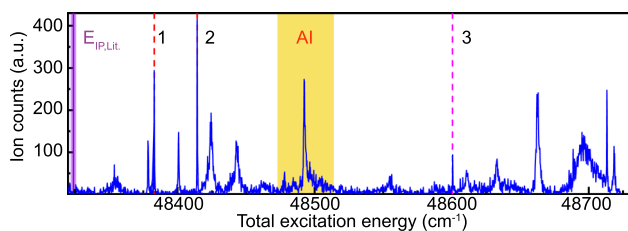
Fig. 3 Measured ionization spectrum of scheme A. The identified AI is highlighted by a yellow box and was used as SES in case of scheme A. The literature value of the IP with $48324(2)\mathrm{cm}^{-1}$ [15] is marked by a purple solid line. The dashed lines indicate FES starting not from the GS but from different initial states [13]

tion of curium. Further detailed characterizations with respect to the saturation behavior, the elemental selectivity or the absolute ionization efficiency of the individual excitation schemes have not been performed so far. The absolute determination of the elemental selectivity and ionization efficiency would require sample materials of calibrated amounts, which were not available for our measurements.

4 Spectroscopic determination of Rydberg convergences

The spectral range of $48000\mathrm{cm}^{-1}$ to $48400\mathrm{cm}^{-1}$ (*cf.* Fig. 4) was spectroscopically investigated for all three excitation schemes A, B and C. Each spectrum was measured twice, scanning the second laser either upwards or downwards with a slight shift of typically $0.1\mathrm{cm}^{-1}$ between the peak positions due to a small delay in the data acquisition. The downwards scans are shown in Fig. 4. The level positions are given as the mean of the two recorded values in Tables 4 and 5. The statistical error is given by the standard deviation of the measured energy positions between upwards and downwards scan as $0.02_{\mathrm{stat}}\,\mathrm{cm}^{-1}$, confirming the reproducibility of the

data. As an additional statistical uncertainty, the fit errors of the FES and SES were added up to this error. The systematic error describes uncertainties of the frequency readout by the wavemeter of $0.12_{\mathrm{sys}}\,\mathrm{cm}^{-1}$. The energy position of the FES and the precision of this wavelength measurement were also taken into account in the systematic uncertainties.

As expected, a specifically high level density just below the IP is clearly visible in Fig. 4 for all three spectra. Hence, configuration interactions are expected and could lead to shifts in energy positions and line intensities, which complicates the determination of Rydberg levels. In general, the limit of the Rydberg series, which corresponds to the IP (E_{IP}) in our case, and the effective principal quantum number n^* of each energy level E_n are linked via the well-known Rydberg–Ritz formula

$$E_n = E_\infty - \frac{R_\mu}{(n - \delta(n))^2} = E_\infty - \frac{R_\mu}{(n*)^2}. \quad (1)$$

The parameters denote the limit E_∞, the reduced-mass Rydberg constant R_μ and the quantum defect $\delta(n)$. Near the IP, Rydberg series are expected to have a constant quantum defect as described by the Ritz expansion, which approaches δ_0 for sufficiently high principal quantum numbers n [24]

$$\delta(n) \approx \delta_0 + \frac{\delta_1}{(n - \delta_0)^2} + \frac{\delta_2}{(n - \delta_0)^4} + ... \quad (2)$$

A δ_0 mod 1 versus n^* plot should thus exhibit an arrangement of the peak positions along horizontal lines corresponding to individual Rydberg series. The constant leading term δ_0 is estimated for curium ($Z = 96$) to be around 5.3, 4.8, 3.8 and 2.0 for s, p, d and f levels, respectively, depending on the orbital angular momentum [25]. The effective principal quantum number n^* of all measured levels was calculated for different E_∞ values, which were chosen in the range of $48320\mathrm{cm}^{-1}$ to $48340\mathrm{cm}^{-1}$ and plotted in a δ_0 mod 1 versus n^* plot. Rydberg series should exhibit a constant quan-
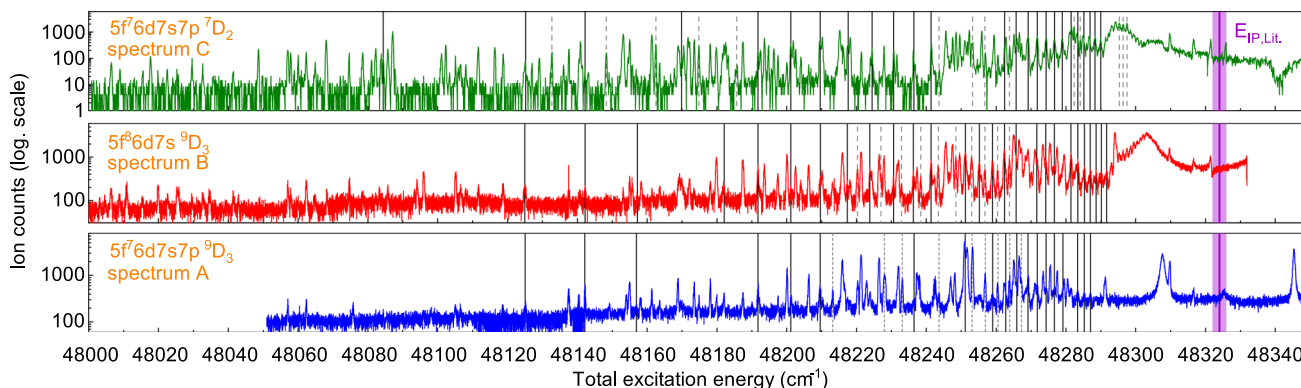

Fig. 4 Measured spectra of schemes A, B and C (*cf.* Fig. 2). The literature value of the IP of $48324(2)\mathrm{cm}^{-1}$ [15] is indicated by a purple line, with the magenta band depicting the 2σ uncertainty. Expected values for Rydberg resonances with a quantum defect of $\delta_0 \approx 0.9$ are marked by a solid line, those with a $\delta_0 \approx 0.5$ by a dashed line
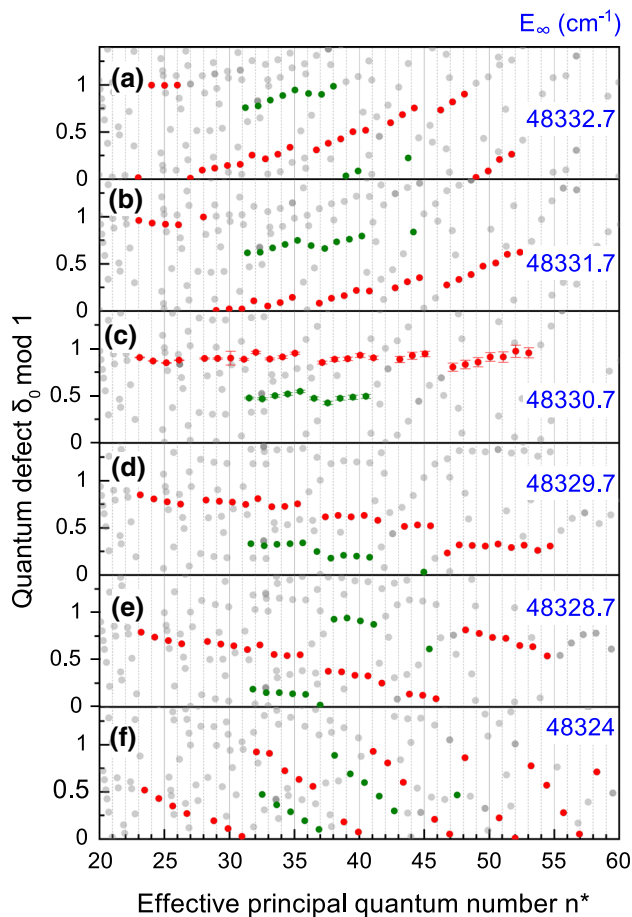
Fig. 5 The quantum defect δ_0 mod 1 versus the effective quantum number n^*, shown for six different ionization limits E_∞. Resonances observed in scheme B are given by gray marked points. Two Rydberg series are identified in plot c) and are marked in green (s-series) and red (d-series) in all plots. Both have a particularly constant $\delta(n)$ slope for the IP of 48330.7cm^{-1}. The error bars indicate the uncertainty, which is dominated by systematics. The six plots illustrate the influence of different ionization limits on the $\delta(n)$ slope; plot f) visualizes the situation for the literature value of the ionization potential (IP)

Fig. 6 The quantum defect δ_0 mod 1 versus the effective quantum number n^* shown for the schemes A, B and C with the ionization limit $E_\infty = 48330.7$ cm^{-1}. The color coding corresponds to the one in Fig. 5

Fig. 7 **a)** Rydberg-Ritz fit of the d-series with δ_0 mod 1 $\approx$ 0.9 from excitation scheme B (red dots) in the range of $n = 27$ up to $n = 57$ with **b)** corresponding residua from the fit

tum defect due to the dominant leading term in Eq. 2 for high n.

Due to the complex spectra with its high line densities, the δ_0 mod 1 versus n^* plot alone did not provide suitable information for a direct assignment of Rydberg states to a specific series. Hence, the resonance lines were compared in regard to their widths and intensities to identify regularities. Rydberg levels obviously affected by perturbations as visible by strong fluctuations in intensity, width and shape compared to their neighbors were not assigned to one Rydberg series and thus not considered in the Rydberg analysis.

Figure 5 shows the influence of the series limit E_∞, indicated in the upper right corner, on the quantum defect plot for spectrum B. For the correct series limit, an a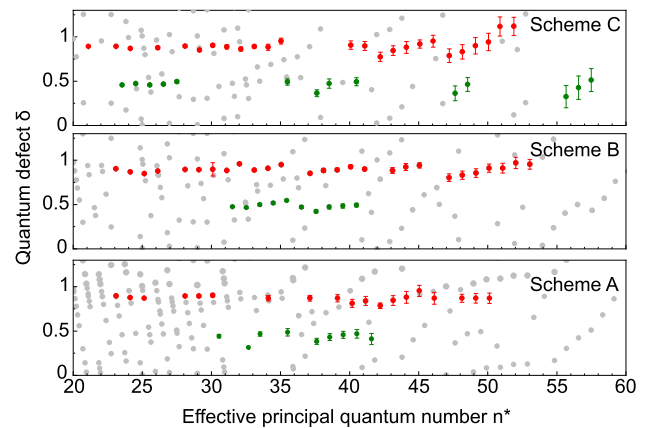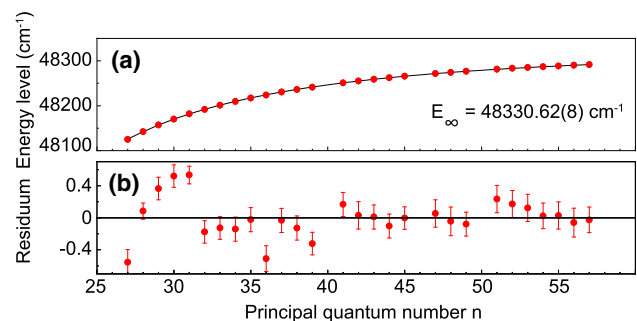rrangement of the data points with horizontal lines of constant quantum defect is expected, which is observed best in Fig. 5 c) for $E_\infty = 48\,330.7$cm^{-1}. For this value, the error bars are also given, which have been omitted in the other five plots for the sake of clarity.

In all excitation schemes, two series at δ_0 mod 1 with $\approx$ 0.9 and $\approx$ 0.5 were identified, shown in Fig. 6 for all three schemes A, B and C under study and for the optimum E_∞ of Fig. 5.

Already a deviation of 1cm^{-1} changes the rather constant $\delta(n)$ progression of c) into a significantly increasing or decreasing slope. A similar situation of constant δ-values could be identified in all the three δ versus n^*-plots (based on spectra A, B and C) for series limit of 48330.7cm^{-1}. In all three spectra, the two Rydberg series were clearly visible with δ_0 mod 1 $\approx$ 0.5 and $\approx$ 0.9. Energetic positions of the identified Rydberg levels including their principal quantum numbers n are listed in Table 4 of the d-series and in Table 5 of the s-series. The further Rydberg analysis was done for these six Rydberg series independently.

The extracted quantum defects were compared with the theoretical values from [25]. Considering the electron configurations and parity of the respective intermediate states, the series with δ_0 mod 1 $\approx$ 0.5 (*cf.*

Table 1 Summary of the series limits $E_{\infty,R}$ determined from Rydberg-Ritz fits of Rydberg series. In each ionization spectrum, two series were identified. The series indicated are given with the number of assigned resonances and the quantum defect δ_0 mod 1

Scheme	Series	n interval	# peaks	δ_0 mod 1	$E_{\infty R}$ [cm^{-1}]
A	d	$27-54$	19	0.90(3)	48331.09(38)
A	s	$36-47$	9	0.40(6)	48330.54(34)
B	d	$27-57$	27	0.879(8)	48330.62(8)
B	s	$37-46$	10	0.50(3)	48330.72(22)
C	d	$25-56$	25	0.884(6)	48330.56(9)
C	s	$29-63$	14	0.470(8)	48330.76(7)

Fig. 5 green series) was identified as s-series. The second Rydberg series with the quantum defect of δ_0 mod $1 \approx 0.9$ (*cf.* Fig. 5 red series) is assigned to a d-series due to parity considerations. In particular, this d-series was strongly influenced by perturbations at quantum numbers $n = 37, 43, 47$, corresponding to 48245cm^{-1}, 48265cm^{-1} and 48280cm^{-1}, respectively, which are well visible in Fig. 5. In all Rydberg series, the occurrence of mixed states cannot be excluded. Exemplarily, a fit of the Rydberg-Ritz formula to the series with δ_0 mod $1 \approx 0.9$ of excitation scheme B is given in Fig. 7 together with the residua, showing the accuracy of the description using Eqs. 1 and 2 and few outliers caused by the perturbations.

An overview of the results for all investigated Rydberg series is given in Table 1. All Rydberg resonances were fitted by Gaussian profiles. All six individually determined E_∞ values are in good agreement within their uncertainties. The weighted average was calculated from the six E_∞ values and their uncertainties, to give the IP, denoted $E_{IP,R}$, with a value of $48330.66(4)_{stat}(12)_{sys}$ cm^{-1}. Due to somewhat vague procedure for the assignment of the Rydberg states in the complex spectra and the significant deviation from the previously reported result of $48324(2)$cm^{-1} Köhler [15], the IP was afterward independently determined by field ionization.

5 Electric field ionization

The saddle point model for electric field ionization (FI) was used as a further method for IP extrapolation since no assignment of individual series and no distinction between Rydberg and other valence states are required. The method is discussed in detail by Littman *et al.* [26]. In order to perform well-controlled electric FI, the first excitation step laser beam was irradiated transversely between the two aperture electrodes U_1 and U_2 of the MABU spectrometer with diameters of 3mm (*cf.* Fig. 1). Here, a well-defined electric field strength could be set by applying a positive voltage to U_1 and a negative voltage to U_2, with both electrodes being precisely installed 1cm apart. The ions produced by surface ionization inside the atomizer were suppressed by U_1. Only neutral species diffused into the ionization region

between U_1 and U_2. The interaction volume of the ionization process was spatially defined by the overlap of the laser beam for excitation of the FES and the laser beam for excitation of the SES, which were arranged in transversal and longitudinal direction, respectively. In this way, ionization no longer takes place inside the atomizer, but exclusively in the intersection region of the two laser beams inside the homogeneous electric field with an electric field strength of $F = (U_1 - U_2)/d$. For each field strength setting, the voltages of electrode U_3, the downstream einzel lens, and the $90°$ quadrupole deflector were optimized to ensure the highest ion beam transmission. This experimental setup for FI has already been successfully used by Studer *et al.* [20] to determine the IP value of promethium.

The electric field reduces the ionization threshold $W_s \backsim IP - \sqrt{F_T}$, with the subscript T denoting the field threshold, at which a highly excited atom is ionized [26,27]. The saddle point W_s of the potential is given by

$$W_s = E_{IP} - 2\sqrt{\frac{Z_{eff}e^3 F_T}{4\pi\epsilon_0}}, \qquad (3)$$

where Z_{eff} is the effective charge of the atomic core. For highly excited states, the ionization threshold can be simplified to $W_s = E_{IP} - 6.12\,(\text{V/cm})^{-1/2} \cdot \sqrt{F_T}$ under the assumption of $Z_{eff} = 1$. Thus, the ionization threshold W_s can be measured for several field strengths for subsequent extrapolation to $F_T = 0$ to determine the IP.

The energy levels of excitation scheme B were used as a starting point for the FI studies due to the higher spectral line density below the ionization potential compared to spectra A and C (*cf.* Fig. 4), as well as the significantly higher count rates. Köhler *et al.* performed field ionization inspecting the range of 48210cm^{-1} − 48290cm^{-1}, while in this work, FI data were taken between 48245cm^{-1} and 48305cm^{-1} and thus closer to the expected $E_{IP,R}$ value. In this way a more reliable and precise extrapolation to zero field is expected.

In an initial experimental approach for FI, the extended range of 48228cm^{-1} up to 48348cm^{-1} was scanned for several applied electric field strengths in the range of $55\,\text{V/cm}$ to $220\,\text{V/cm}$. Four spectra for the cases of $F = 55, 70, 140$ and $220\,\text{V/cm}$ are given in
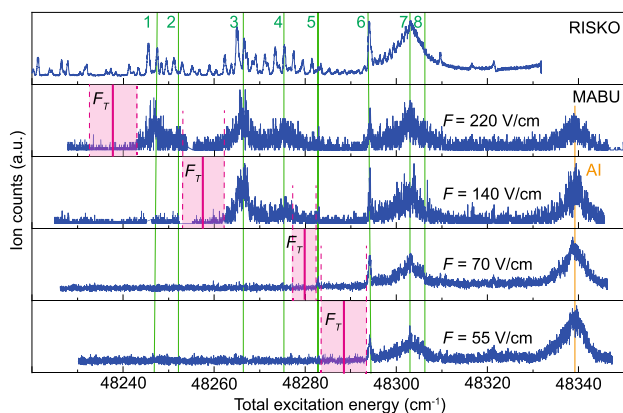
Fig. 8 Spectroscopic studies of FI using scheme B. Scans at different fixed electric fields at MABU in comparison to a spectrum from RISIKO with ionization in the atomizer are given. The dashed line marks the last measured and the next expected energy level. The F_T is located between both resonances and its expected position is marked by a solid line. The F_T was measured independently for fixed wavelengths marked with a green solid line and numbered by variation of the field strength with fixed laser excitation at this position. The reference AI is shown with a orange solid line
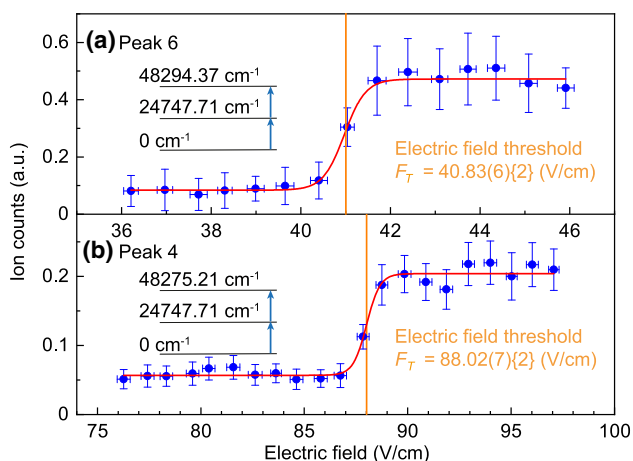
Table 2 Eight energy levels W_s situated just below the ionization potential for which the electric field ionization thresholds $F_T^{1/2}$ were determined. For the latter, round braces indicate the statistical errors and curly braces the systematic errors

#	W_s (cm^{-1})	$F_T^{1/2}$ (V/cm)$^{1/2}$
1	48246.64(28)	14.454(4){1}
2	48251.86(28)	13.173(5){1}
3	48265.83(27)	10.909(3){1}
4	48275.21(29)	9.382(4){1}
5	48282.81(21)	8.546(10){1}
6	48294.37(28)	6.390(5){2}
7	48304.30(21)	5.482(20){3}
8	48303.21(21)	4.118(9){2}

Fig. 9 Step function of the F_T for the energy levels 48294.37cm^{-1} in a) and 48275.21cm^{-1} in b). The indicated reversal points of the sigmoid fit (red line, error band orange) correspond to the F_T. The round braces indicate the statistical errors and curly braces the systematic errors

Fig. 8. The plot is complemented by a spectrum from RISIKO, taken in collinear geometry, where also all Rydberg levels below the IP are ionized due to the conditions in the hot cavity. In contrast, only energy levels above the ionization threshold were ionized using the FI setup at MABU. The ionization threshold lies between the last measured and the next expected energy level, marked by dashed lines and the shaded area in the spectra. These data did not deliver a conclusive database for an IP fit with reasonable precision. Thus, in a second approach, the ionization threshold was measured by successively fixing the laser excitation to a fixed wavelength and in each case varying the electric field strength F. In this way, the ionization threshold was measured for eight different energy levels between 48245.9cm^{-1} and 48304.30cm^{-1}, which are marked by the green solid lines in Fig. 8. After each scan, a reference scan was performed using the AI state at 48338.11cm^{-1} for correction of the threshold data. The ion signal of an AI state is not sensitive to the weak electric fields and therefore this reference scan maps the ion optics transmission for the respective field scan. Two examples for measurements of such electric field ionization threshold measurements are given in Fig. 9 a) and b). The data are described by a sigmoid function

$$S(F) = A_0 + \frac{A_1}{1 + e^{-k(F-F_T)}} \qquad (4)$$

with the offset A_0, the amplitude A_1 as well as the turning point F_T, which can be understood as the ionization threshold for the expected resonance, assuming the laser excitation is centered on the respective transition [20]. F_T was thus obtained for eight energy levels and is given in Table 2.

For these studies, systematic errors were similar as in the case of the Rydberg measurements and were described specifically for the electric field ionization in detail in [20]. Further errors results in 0.2 cm^{-1}, including the wavemeter uncertainty of 0.12_{sys} cm^{-1} and the laser fluctuations of 0.08_{stat} cm^{-1} during the measurements. The estimation of ΔF_T turned out to be more complicated. The systematic error includes the distance uncertainty between U_1 and U_2 of 1% and influences by the field leakage through the transmission holes. The statistical error was set as the standard deviation of the voltage values during the measurements. Including the fit error this amounts to about $10^{-1} - 10^{-2}$ V for a measured threshold. The uncertainties given in Table 2 include the statistical and systematic errors.

For IP determination, W_s was plotted against $F_T^{1/2}$ (*cf.* Fig. 10). The data points 1-6 can be described very accurately by a linear function with the values 7 and 8 at lowest electric fields showing slight deviations
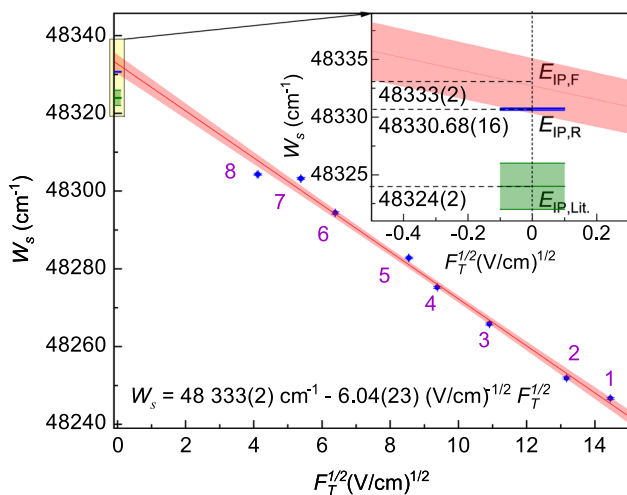
Fig. 10 Extracted ionization thresholds plotted against the square root of the field strength $F_T^{1/2}$. The ionization limit can be determined from the y-axis intersection. The bright red area indicates the confidence interval for the linear fit, including the x and y errors equally. The inset shows a more detailed view on the W_s-intersection. The values $E_{\mathrm{IP,F}}$ and $E_{\mathrm{IP,R}}$ agree within the limits of their errors

Table 3 Overview of the ionization potentials (IPs) determined in this work ($E_{\mathrm{IP,R}}$, $E_{\mathrm{IP,FI}}$ and $E_{\mathrm{IP,av.}}$) in comparison to $E_{\mathrm{IP,Lit.}}$

		$E_{\mathrm{IP}}\,(\mathrm{cm}^{-1})$
$E_{\mathrm{IP,R}}$	This work	48330.66(16)
$E_{\mathrm{IP,FI}}$	This work	48333(2)
$E_{\mathrm{IP,av.}}$	This work	48330.68(16)
$E_{\mathrm{IP,Lit.}}$	[15]	48324(2)

Table 4 Measured Rydberg resonances of spectra A, B and C. The principal quantum number is given for each energy level. The series were assigned based on Fano *et al.* [25], in this case as a d-series. The uncertainties include the fit errors as well as the systematic and statistical errors (*cf.* Ch. 4)

n	$E_\mathrm{A}\ (\mathrm{cm}^{-1})$	$E_\mathrm{B}\ (\mathrm{cm}^{-1})$ $d-$series	$E_\mathrm{C}\ (\mathrm{cm}^{-1})$
25	–	–	48084.37(1)
26	–	–	
27	48125.08(14)	48124.97(16)	48125.16(14)
28	48142.10(9)	48142.25(12)	48142.25(14)
29	48156.93(14)	48157.23(14)	–
30	–	48170.43(14)	48169.89(21)
31	–	48182.07(11)	–
32	48191.76(17)	48191.76(14)	48191.76(14)
33	48201.15(16)	48201.17(15)	48201.34(17)
34	48209.56(15)	48209.60(15)	48209.54(15)
35	–	48217.36(16)	48217.33(17)
36	–	48223.81(15)	48224.44(15)
37	–	48230.60(15)	48230.60(11)
38	48236.49(17)	48236.28(14)	48236.42(19)
39	–	48241.37(15)	48241.36(17)
40	48251.10(14)	–	–
41	–	48251.17(17)	–
42	–	48255.16(15)	–
43	48259.03(15)	48258.95(15)	–
44	48262.75(15)	48262.36(14)	48262.43(16)
45	48265.92(16)	48265.73(17)	48265.75(16)
46	48269.12(9)	–	48269.15(15)
47	48271.78(15)	48271.67(18)	48271.78(16)
48	48274.32(17)	48274.21(15)	48274.32(17)
49	48276.62(15)	48276.64(17)	48276.70(11)
50	48279.03(15)	–	48278.95(15)
51	–	48281.43(17)	48281.47(16)
52	48283.32(9)	48283.40(17)	48283.40(16)
53	48285.24(10)	48285.26(17)	48285.18(17)
54	48287.03(10)	48286.96(16)	48286.91(17)
55	–	48288.66(17)	48288.31(18)
56	–	48290.16(18)	48289.93(16)
57	–	48291.70(16)	–

from the straight line. Shifting and splitting of spectral lines could be caused by the Stark effect. Nevertheless, this influence should be smallest for the weakest field strengths. Additionally, the influence of the Stark effect was checked by measuring specific energy levels at different electric fields and comparing their spectral position. No measurable shift, line broadening or splitting could be observed. This indicates that the Stark effect has no significant influence on the position of the measured turning points for individual resonances. A reason for the deviations of the values of data points 7 and 8 is seen in the fact, that in comparison to Studer *et al.* [20], larger apertures were used for both electrodes U_1 and U_2. Thus, the measurements of the ionization thresholds of data points 7 and 8 could have been influenced by variations in the ion optical settings and according to changes in the stray fields, which most strongly affect small F settings. Overlapping signals from neighboring broad resonances could additionally contribute; point 8, e.g., was measured on a signal maximum consisting of several resonances.

The data were described by a linear function, fitted according to Deming regression [28]. This linear regression method is based on a maximum likelihood estimation of the regression parameters. The residuals of the x and y values are both assumed to be independent and normally distributed. Finally, the y-axis intercept corresponds to the IP yielding a value of $48333(2)\,\mathrm{cm}^{-1}$. The slope of the linear function is $-6.04(23)\,(\mathrm{V/cm})^{-1/2}$ perfectly confirming the expectation of $-6.12\,(\mathrm{V/cm})^{-1/2}$ [20].

6 Conclusion

Two-step RIS was applied for sensitive atomic spectroscopy of curium ($Z = 96$), using minuscule samples in the ng range. Three different FES were used to inves-

Table 5 Measured Rydberg resonances of spectra A, B and C. The principal quantum number is given for each energy level. Series assignment was according to Fano et al. [25], in this case as a $s-$series. The uncertainties include the fit errors as well as the systematic and statistical errors (*c.f.* Ch. 4)

n	E_A (cm^{-1})	E_B (cm^{-1})	E_C (cm^{-1})
$s-$series			
29	–	–	48132.70(15)
30	–	–	48148.30(18)
31	–	–	48162.51(16)
32	–	–	48174.84(15)
33	–	–	48185.65(20)
34	–	–	–
35	–	–	–
36	48213.18(15)	–	–
37	–	48220.28(15)	–
38	48227.98(15)	48227.02(15)	–
39	48233.11(14)	48232.92(16)	–
40	–	48238.41(16)	–
41	48243.69(20)	48243.34(14)	48243.67(17)
42	–	48248.46(15)	–
43	48253.15(14)	48252.98(15)	48253.23(16)
44	48256.93(15)	48256.77(16)	48256.77(20)
45	48260.51(14)	48260.43(16)	–
46	48263.90(16)	48263.82(15)	48263.82(15)
47	48267.26(19)	–	–
48	–	–	–
49	–	–	–
50	–	–	–
51	–	–	–
52	–	–	–
53	–	–	48282.34(17)
54	–	–	48284.12(15)
55	–	–	–
56	–	–	–
57	–	–	–
58	–	–	–
59	–	–	–
60	–	–	–
61	–	–	48295.30(16)
62	–	–	48296.41(16)
63	–	–	48297.50(15)

tigate high lying Rydberg series below as well as AI resonances above the IP.

Within all three excitation schemes, in total six Rydberg series were identified and were assigned to a *d*-series in the range of $n = 25 - 57$ and a *s*-series with $n = 29 - 63$. Based on these Rydberg convergences, an IP value of $E_{IP,R} = 48330.68(12)$cm^{-1} was determined. FI was used as a complementary and independent method to determine the IP by using the saddle point method. The ionization threshold was determined for eight energy levels below the IP, resulting in an IP value of $E_{IP,FI}$ with $48333(2)$cm^{-1}. The results of this work, as well as the previous literature value, are shown in Table 3. As expected, the precision of the Rydberg

analysis is one order of magnitude higher than the one of FI determination.

Considering the combined uncertainties of $E_{IP,R}$ and $E_{IP,FI}$, the two values are in good agreement. Finally, the IP was determined by the weighted average of both values as $E_{IP,av.}$ to be $48330.68(16)$cm^{-1}. The good agreement between the two independent measurement methods gives us confidence in our results, which we propose as a correction to the Köhler *et al.* value [15].

Author contributions

References

1. G.T. Seaborg, Science **104**, 379-386 (1946), https://www.science.org/doi/10.1126/science.104.2704.379
2. R. A. James *Isotopes of the New Element, Curium (Atomic No. 96)* (PhD. thesis, University of California, 1948), https://escholarship.org/uc/item/9zt6g894
3. Gregg J. Lumetta, et al. "Curium." The chemistry of the actinide and transactinide elements. Springer, Dordrecht, 1397-1443 (2008), https://link.springer.com/content/pdf/10.1007/1-4020-3598-5_9.pdf
4. A. Habibi et al., Radioanal. Nucl. Chem. **329**, 545–554 (2021). https://doi.org/10.1007/s10967-021-07751-7
5. E. Hom et al., Radioanal. Nucl. Chem. **252**, 211–214 (2002). https://doi.org/10.1023/A:1015786431984

6. D. Gorietti et al., Radioanal. Nucl. Chem. **314**, 1785–1792 (2017). https://doi.org/10.1007/s10967-017-5553-y
7. H. Bosco et al., Hyperfine Interact. **241**, 1–8 (2020). https://doi.org/10.1007/s10751-020-1696-2
8. M. Franzmann et al., Anal. Spectrom. **33**, 730–737 (2018). https://doi.org/10.1039/C7JA00423K
9. N. Kneip et al., Hyperfine Interact. **241**, 1–7 (2020). https://doi.org/10.1007/s10751-020-01712-4
10. S. Raeder et al., Radiochim. Acta **107**, 645–652 (2019). https://doi.org/10.1515/ract-2019-0001
11. L.R. Morss et al., *The chemistry of the actinide and transactinide elements* (Springer, Dordrecht, 2008)
12. E. F. Worden, et al., J. Opt. Soc. Am., **66**, 109-121 (1976) https://opg.optica.org/josa/abstract.cfm?URI=josa-66-2-109
13. E.F. Worden et al., At. Data Nucl. Data Tables **18**, 459–495 (1976). https://doi.org/10.1016/0092-640X(76)90014-0
14. J. Sugar, J. Chem. Phys. **60**, 4103 (1974). https://doi.org/10.1063/1.1680874
15. S. Köhler et al., Spectrochim. Acta B **52**, 717–726 (1997). https://doi.org/10.1016/S0584-8547(96)01670-9
16. T. Kieck et al., Nucl. Instrum. Methods Phys. Res., B **945**, 1–10 (2019). https://doi.org/10.1016/j.nima.2019.162602
17. K. Zhang et al., PRL **125**, 7–14 (2020). https://doi.org/10.1103/PhysRevLett.125.073001
18. A. Teigelhöfer et al., Hyperfine Interact. **196**, 161–168 (2010). https://doi.org/10.1007/s10751-010-0171-x
19. A. Sonnenschein et al., Hyperfine Interact. **227**, 113–123 (2014). https://doi.org/10.1007/s10751-013-1000-9
20. D. Studer et al., Phys. Rev. A **99**, 1–8 (2019). https://doi.org/10.1103/PhysRevA.99.062513
21. E.F. Worden, J.G. Conway, J. Opt. Soc. Am **66**, 109–121 (1976). https://doi.org/10.1364/JOSA.66.000109
22. J. Blaise, J.-F. Wyart, *Energy levels and atomic spectra* (Tables Internationales de Constantes, Paris, 1992)
23. H. Bosco et al., Sci. Adv. **7**, 1–8 (2021). https://doi.org/10.1126/sciadv.abj1175
24. W. Ritz, Annalen der Physik **317**, 444–446 (1903)
25. U. Fano et al., Rev. Mod. Phys. **48**, 49–68 (1976). https://doi.org/10.1103/RevModPhys.48.49
26. M.G. Littman et al., Phys. Rev. Lett. **41**, 103–107 (1978). https://doi.org/10.1103/PhysRevLett.41.103
27. B.H. Bransden et al., *Physics of atoms and molecules* (Prentice Hall, Harlow, 2003)
28. R. F. Martin, Clin. Chem. **46**, 100-104 (2000), https://academic.oup.com/clinchem/article/46/1/100/5670706